Research article

Irina Volkovskaya*, Lei Xu, Lujun Huang, Alexander I. Smirnov, Andrey E. Miroshnichenko and Daria Smirnova

Multipolar second-harmonic generation from high-Q quasi-BIC states in subwavelength resonators

Abstract: We put forward the multipolar model which captures the physics behind linear and nonlinear response driven by high-quality (high-Q) supercavity modes in sub-wavelength particles. We show that the formation of such trapped states associated with bound states in the continuum (quasi-BIC) can be understood through multi-polar transformations of coupled leaky modes. The quasi-BIC state appears with increasing the order of the dominating multipole, where dipolar losses are completely suppressed. The efficient optical coupling to this state in the AlGaAs nanodisk is implemented via azimuthally polarized beam illumination matching its multipolar origin. We establish a one-to-one correspondence between the standard phenomenological non-Hermitian coupled-mode theory and multipolar models. The derived multipolar composition of the generated second-harmonic radiation from the AlGaAs nanodisk is then validated with full-wave numerical simulations. Back-action of the second-harmonic radiation onto the fundamental frequency is taken into account in the coupled nonlinear model with pump depletion.

A hybrid metal-dielectric nanoantenna is proposed to augment the conversion efficiency up to tens of per cent due to increasing quality factors of the involved resonant states. Our findings delineate novel promising strategies in the design of functional elements for nonlinear nanophotonics applications.

1 Introduction

Controlling light at the nanoscale has been a vibrant field of research for many years motivated by its various applications for optical nanoantennas, integrated photonic circuitry, optical computing, and high-speed ultrathin photonic devices [1–5]. High-index dielectric nanoparticles have emerged as a promising platform to enhance light–matter interactions at the nanoscale based on optically induced electric and magnetic Mie-type resonances [4, 5]. Due to the strong near-field confinement and tailorable field distributions in the subwavelength regime, optically resonant dielectric nanostructures offer powerful tools to facilitate various nonlinear processes including nonlinear frequency conversion, wave mixing, and ultrafast all-optical switching [4, 6–11]. Resonant mechanisms of light localization in dielectric nanostructures, such as magnetic dipole resonance [12–14], nonradiating anapole state [15–17], magnetic Fano resonance [18, 19], and topologically protected edge states [20, 21], have been widely utilized for applications of nonlinear nanophotonics, such as nanoscale light sources [22], imaging [23], sensing, and advanced optoelectronic devices [3].

Methods typically employed to describe nonlinear harmonic generation at the nanoscale are based on the multipolar decomposition of the fields in spherical multipoles [4, 24–27]. This approach provides a transparent interpretation for the measurable far-field characteristics, such as

*Corresponding author: Irina Volkovskaya, Institute of Applied Physics, Russian Academy of Science, Nizhny Novgorod 603950, Russia, E-mail: volkovskaya@ipfran.ru
Lei Xu: School of Engineering and Information Technology, University of New South Wales, Canberra, ACT 2600, Australia; Advanced Optics and Photonics Laboratory, Department of Engineering, School of Science & Technology, Nottingham Trent University, Nottingham NG11 8NS, UK
Lujun Huang and Andrey E. Miroshnichenko: School of Engineering and Information Technology, University of New South Wales, Canberra, ACT 2600, Australia
Alexander I. Smirnov: Institute of Applied Physics, Russian Academy of Science, Nizhny Novgorod 603950, Russia
Daria Smirnova: Institute of Applied Physics, Russian Academy of Science, Nizhny Novgorod 603950, Russia; Research School of Physics, The Australian National University, Canberra, ACT 2601, Australia

conversion efficiency and radiation patterns, since they are essentially determined by the interference of dominating multipolar modes [4]. The nonlinear response depends on both incident polarization and symmetry of the specific material or composite structures, such as nanoparticle oligomers [27–29]. For instance, the nonlinear response of disk-shaped nanoantennas made of noncentrosymmetric III–V semiconductors (GaAs or AlGaAs) grown along (100), (110), and (111) crystallographic directions exhibits four-fold, two-fold, and continuous rotational symmetries, respectively [26, 30]. Specifics of the radiation characteristics in each case can be explained by different parities of nonlinearly generated multipoles, so-called nonlinear multipolar interference. This represents an example where multipolar analysis has been proven to be a useful instrument for design of directional nonlinear light emission [31].

A recently suggested approach to trap light in individual subwavelength dielectric nanoresonators is based on high-quality supercavity modes associated with the physics of quasi-bound states in the continuum (quasi-BIC) [32–34]. These states are in some sense similar to BICs in infinite periodic dielectric structures: their high finesse is due to the destructive interference of several far-field radiation channels. Two interpretations of quasi-BIC formation in an open resonator, based on (i) leaky modes supported by the particle [33] and (ii) multipoles of the electromagnetic field [35], were discussed; however, no direct correspondence between these two models has been established up to now. Lately, it has been proposed to utilize these high-quality states to enhance the classical nonlinear process of second-harmonic generation in dielectric nanodisks [36].

In this paper, we develop a comprehensive multipolar theory of the second-harmonic generation (SHG) from high-quality quasi-BIC states in an AlGaAs cylindrical nanoresonator (nanodisk). The process of SHG is schematically illustrated in Figure 1. We show that the formation of quasi-BIC states can be naturally understood through multipolar transformations of coupled leaky axially symmetric modes supported by the nanodisk. The strong SHG can be expected in the case of efficient excitation of the mode with the high quality factor. To achieve efficient coupling to the mode at the pump frequency, the multipolar composition of the pump source should match the multipolar composition of this mode. We show that the azimuthally polarized beam can be used to couple to the quasi-BIC state most efficiently because it contains magnetic multipoles with zero azimuthal numbers only that matches the quasi-BIC multipolar origin and maximizes the modal overlap. Analyzing the spatial distribution of the induced nonlinear source with the approach put forward in

our earlier works [25, 26], we reveal that the complex multipolar composition of the second-harmonic radiation coincides with the multipolar composition of a particular high-quality eigenmode of the disk at the second-harmonic (SH) frequency. We obtain that the efficiency of SHG is strongly enhanced up to several per cent, provided the generated frequency matches the supported resonance, for parameters of the nanoresonator corresponding to the nearly resonant excitation of the quasi-BIC state at the fundamental frequency (FF). We perform full-wave numerical simulations of SHG taking into account nonlinear effects of back-action and propose the BIC-inspired design of a hybrid metal-dielectric nanoantenna where the effect of pump depletion is further increased suggesting a promising application for the frequency downconversion.

2 Results and discussion

2.1 Multipolar model of quasi-BIC formation

We consider a high-index cylindrical dielectric resonator that supports leaky modes (modes of an open resonator) that may hybridize (couple) when tuning geometric
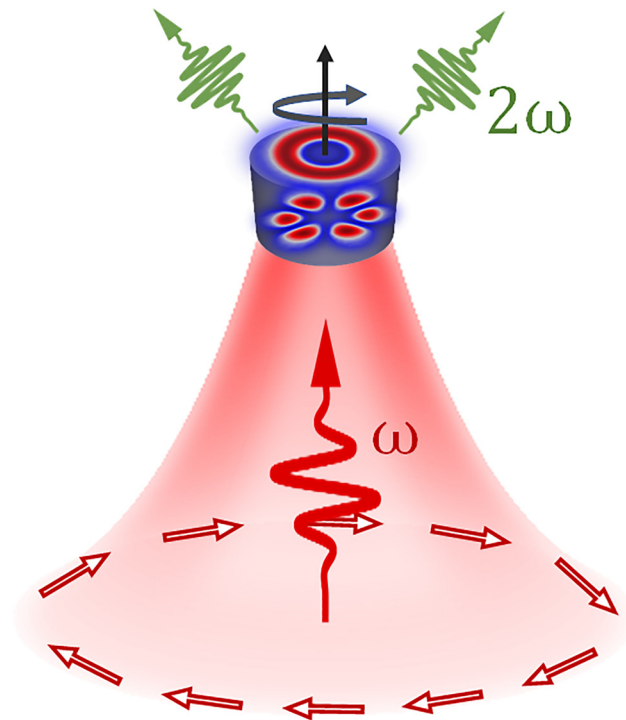

Figure 1: Schematic of the geometry. Azimuthally polarized cylindrical vector beam of frequency ω excites an axially symmetric supercavity mode in the nanodisk. As a result of nonlinear interaction, the second-harmonic light of 2ω is generated.

parameters. The particle is characterized by a frequency-dependent dielectric permittivity $\varepsilon(\omega)$ and is surrounded by a homogeneous host medium with $\varepsilon_h = 1$. The harmonic time dependence of the fields in the form $e^{i\omega t}$ is implied.

Here, we focus on rotationally symmetric TE-polarized modes in the cylindrical coordinate system (E_φ, H_ρ, H_z), whose electromagnetic field does not depend on the azimuthal angle φ. With the use of the finite element method (FEM) in COMSOL Multiphysics, we perform the eigenmode analysis numerically and plot dispersion as a function of the normalized geometric parameters defined as the disk aspect ratio r/h and the size parameter r/λ_0, where λ_0 is the mode wavelength. The size parameter defined as a ratio of the disk radius to the mode wavelength can also be referred to as a normalized eigenfrequency. The results of calculations for the AlGaAs nanodisk with the fixed height $h = 645$ nm are summarized in Figure 2. Two dispersion curves depicted as colored dots exhibit characteristic avoided crossing in the plane of parameters, which is a signature of the strong-coupling regime. It is accompanied by modification of the modes quality factors and formation of the quasi-BIC state that can be naturally understood through
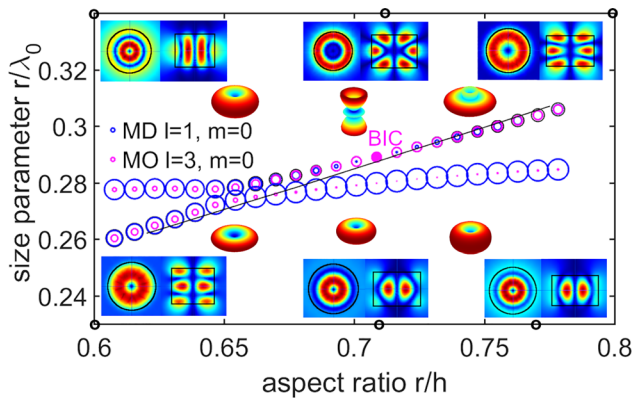

Figure 2: Dispersion of the axially symmetric eigenmodes of the AlGaAs nanodisk. Colored circles depict the multipolar decomposition of these modes: magnetic dipole (MD – blue) and magnetic octupole (MO – pink), sizes of circles scale their relative contributions and radiative decay. The upper branch traces the high-quality mode and features a special point in the parameter space ($r/h = 0.71$, $r/\lambda_0 = 0.29$), where the quality factor of this mode reaches its maximum. The filled pink dot marks this quasi-BIC point, it corresponds to pure MO. Insets show near-field distributions of the electric field magnitude and far-field diagrams: the top row corresponds to the high-quality mode at $r/h = 0.6$, 0.71 (BIC), 0.8; the bottom row corresponds to the low-quality mode at $r/h = 0.6$, 0.71, 0.77. The corresponding values of aspect ratio are marked by dots at the horizontal axis. The overlaid black line sketches a dispersion branch of the mode near the second-harmonic frequency (the wavelength is doubled for direct comparison).

multipolar transformations of coupled modes as we describe below.

For a nonspherical shape of the resonator, the interacting modes can be in general viewed as a superposition of the spherical multipoles distinguished by orbital l and azimuthal m indices. Multipolar analysis of the considered TE-polarized axially symmetric eigenmodes suggests that the basis of parent multipoles mainly consists of a longitudinal magnetic dipole (MD) $l = 1$, $m = 0$ and a magnetic octupole (MO) $l = 3$, $m = 0$ so that each mode has two multipolar radiation channels, dipolar and octupolar. In Figure 2, sizes of circles illustrate their relative contributions in multipolar expansions of the modes (line plots are provided in Supplementary Material). The occurrence of high-Q supercavity mode is accompanied by an increase in the order of a dominating multipole from $l = 1$ (MD) to $l = 3$ (MO) and corresponds to the pure magnetic octupole. In the quasi-BIC condition ($r/h = 0.71$ and $r/\lambda_0 = 0.29$), two magnetic dipoles interfere destructively in the coupling to the octupole, thus, restoring its high-quality factor. Insets show how the electric field distributions inside the disk and far-field diagrams of these modes change as we move along the dispersion curves. While far from the BIC point, the radiation patterns are dipolar, near the BIC point the pattern of the high-Q mode turns to the rotationally symmetric magnetic octupole with three lobes. In addition, the black line in Figure 2 shows the dispersion of the mode near the second-harmonic frequency. The eigenmode analysis is performed for the AlGaAs disk taking into account the material dispersion. The refractive index in the fundamental wavelength range 1500–1700 nm $n(\omega) = \sqrt{10.73} \approx 3.27$ and in the SH wavelength range 750–850 nm $n(2\omega) \approx 3.52$ [37].

We then corroborate our rigorous numerical results by an analytical model setting the correspondence of the non-Hermitian coupled-mode theory and the multipolar analysis. Coupling of two leaky eigenmodes shown in Figure 2 can be described by the Hamiltonian [33, 34]

$$\widehat{H}_2 = \begin{pmatrix} E_1 & V \\ W & E_2 \end{pmatrix}, \qquad (1)$$

being a square matrix, where $E_1 = \tilde{\omega}_1 + i\gamma_1$ and $E_2 = \tilde{\omega}_2 + i\gamma_2$ are complex frequencies of the modes 1 and 2, W and V are complex coupling parameters including the interaction between the modes via free space, $W \neq V^*$. A scheme of this phenomenological two-level model is shown in Figure 3A. The eigenfrequencies depend on the aspect ratio $\xi \equiv r/h$ and can be deviated from the point $\tilde{\omega}_{1,2} = 0$. Taking $\gamma_1 = \gamma_2 = \gamma$, $V = W = \varkappa + i\gamma$, in the strong-coupling regime $\gamma \lesssim \varkappa$, the eigenvalues of the matrix 1 are given by $E_+ = \varkappa + 2i\gamma$ and $E_- = -\varkappa$, that yields a frequency splitting of $2\varkappa$ and the infinitely-large Q factor for one of the modes
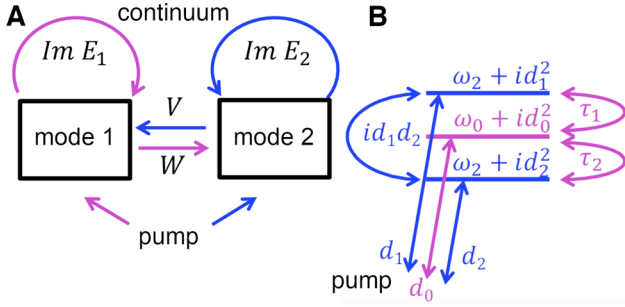
Figure 3: (A) Schematic of interaction between two-coupled eigenmodes of an open dielectric resonator. Arrows illustrate individual couplings of the modes to the continuum and couplings between the modes via the continuum. (B) Schematic of the three-level multipolar model for the formation of the quasi-BIC state captured by the Hamiltonian Eq. (6).

(BIC state). The avoided crossing of two modes in the two-level system qualitatively captures the numerically calculated dispersion depicted in Figure 2.

For our system, we derive the dynamic equations for two modes with slowly varying amplitudes B_1 and B_2 excited by the external pump source in the following form:

$$\frac{d}{dt}\begin{pmatrix} B_1 \\ B_2 \end{pmatrix} - i\hat{H}_2 \begin{pmatrix} B_1 \\ B_2 \end{pmatrix} = \begin{pmatrix} d_1 S_d + d_{01} S_0 \\ d_2 S_d + d_{02} S_0 \end{pmatrix} e^{i\Omega t}, \quad (2)$$

where the matrix $\hat{H}_2$ explicitly reads

$$\hat{H}_2 = \begin{pmatrix} \tilde{\omega}_1(\xi) + i[d_1^2 + d_{01}^2] & \varkappa + i[d_1 d_2 + d_{01} d_{02}] \\ \varkappa + i[d_1 d_2 + d_{01} d_{02}] & \tilde{\omega}_2(\xi) + i[d_2^2 + d_{02}^2] \end{pmatrix}. \quad (3)$$

The d coefficients govern both the dipolar and octupolar radiative decays of the modes and their coupling to each other and to the external field, $d_{01,02}^2 \ll d_{1,2}^2$. The near-field coupling is incorporated by off-diagonal $\varkappa$ terms. Using the scattering-matrix method (see Supplementary Material), the coupled-mode equations can be mapped onto the three-state model schematically illustrated in Figure 3B. The reduced multipolar basis includes two magnetic-dipole states $a_{1,2}$ and the magnetic-octupole state a_3 with $m = 0$. The evolution equations recast as

$$-i\frac{d\mathbf{a}}{dt} = \hat{H}_3\mathbf{a} - i\mathbf{s}e^{i\Omega t}, \quad (4)$$

with the amplitude column-vector $\mathbf{a} = [a_1, a_2, a_3]$, and the external source

$$\mathbf{s} = \begin{pmatrix} d_1 s_d \\ d_2 s_d \\ d_0 s_0 \end{pmatrix}. \quad (5)$$

The non-Hermitian Hamiltonian of the structure in Eq. (4) assumes the form

$$\hat{H}_3 = \begin{pmatrix} \omega_1 + id_1^2 & id_1 d_2 & \tau_1 \\ id_1 d_2 & \omega_2 + id_2^2 & \tau_2 \\ \tau_1 & \tau_2 & \omega_0 + id_0^2 \end{pmatrix}, \quad (6)$$

where $d_{1,2,0}$ are the effective dipole and octupole moments. The τ coefficients describe the hybridization of the dipole and octupole multipoles. Ohmic losses are neglected. The high-quality resonant state is formed at the frequency $\omega_{BIC} = (\omega_1 d_2 \tau_2 + \omega_2 d_1 \tau_1)/(d_1 \tau_1 + d_2 \tau_2)$, where the imaginary part of the octupole-like eigenstate frequency is restored to a bare value d_0^2.

The excitation of the quasi-BIC mode depends on how efficiently the incident source couples to the BIC state, that is on their spatial overlap. The external source can be divided into the octupolar component S_0 and the dipolar component S_d and their fractions determine the resultant response. We consider two types of pump radiation which carry H_z component of the electromagnetic field and can excite the quasi-BIC mode: a linearly polarized plane wave $\mathbf{E} = E_0 e^{ikx}\hat{\mathbf{y}}$ (PW) and an azimuthally polarized cylindrical vector beam (AP) [38] (see Supplementary Material). We perform the multipolar decomposition of the incident radiation in terms of vector spherical harmonics (see Supplementary Material) and after numerical integration we obtain the following relations of the magnetic octupolar and magnetic dipolar contributions: $\left|\frac{A_M(3,0)}{A_M(1,0)}\right|^2 = 0.875$ for the PW excitation, and $\left|\frac{A_M(3,0)}{A_M(1,0)}\right|^2 = 4.854$ for AP excitation. Remarkably, an AP vector beam can be used to couple to the BIC mode more efficiently than a linearly polarized plane wave because the AP beam can be decomposed solely to magnetic multipoles with $m = 0$ that matches the multipolar composition of the modes, while the plane wave consists of electric and magnetic multipoles with different azimuthal indices m. Furthermore, the relative contribution of MO is significantly higher in the AP vector beam than in the plane wave, so that the azimuthally polarized cylindrical vector beam is favorable for excitation of the high-quality resonance in the dielectric nanodisk. Thus, hereafter we focus on the study of SHG in a AlGaAs nanodisk excited by an AP cylindrical vector beam in the vicinity of the BIC point.

2.2 Nonlinear response driven by quasi-BIC state

For noncentrosymmetric materials, the induced nonlinear polarization is defined by the second-order polarizability tensor $\hat{\chi}^{(2)}$:

$$\mathbf{P}^{(2\omega)} = \varepsilon_0 \widehat{\chi}^{(2)} \mathbf{E}^{(\omega)} \mathbf{E}^{(\omega)}, \tag{7}$$

where ε_0 is the vacuum dielectric constant, $\mathbf{E}$ is the electric field inside the particle. For AlGaAs in the principal axis system of the crystal, the tensor of the second-order nonlinear susceptibility contains only off-diagonal elements $\chi_{ijk}^{(2)} = \chi^{(2)} = 100$ pm/V being nonzero if any of two indices i, j, k do not coincide. Thus, the induced nonlinear polarization at the second-harmonic frequency takes the form

$$\begin{pmatrix} P_x^{(2\omega)} \\ P_y^{(2\omega)} \\ P_z^{(2\omega)} \end{pmatrix} = 2\varepsilon_0 \chi^{(2)} \begin{pmatrix} E_y^{(\omega)} E_z^{(\omega)} \\ E_x^{(\omega)} E_z^{(\omega)} \\ E_x^{(\omega)} E_y^{(\omega)} \end{pmatrix} \tag{8}$$

We assume that the main axes of the crystalline lattice are oriented along the axis of the Cartesian coordinate system: [100] ∥ $\widehat{\mathbf{x}}$, [010] ∥ $\widehat{\mathbf{y}}$, [001] ∥ $\widehat{\mathbf{z}}$. Thereby, in the case of excitation of the azimuthally polarized modes inside the nanodisk the nonlinear current at the second-harmonic frequency has the form

$$\mathbf{j}^{(2\omega)} = 2i\omega\mathbf{P}^{(2\omega)} = 2i\omega\varepsilon_0\chi^{(2)} E_\varphi^{(\omega)2} \sin 2\varphi \widehat{\mathbf{z}}. \tag{9}$$

Here, $E_\varphi^{(\omega)}$ is the electric field distribution inside the particle, which can be approximated by the following expression

$$E_\varphi^{(\omega)} \approx B_1\alpha_1 J_1\left(k_0\sqrt{\varepsilon}\,\rho\right) + B_2\alpha_2 J_1\left(k_0\rho\sqrt{\varepsilon - \frac{\pi}{k_0 h}}\right)\cos\frac{\pi z}{2h}, \tag{10}$$

where J_1 is the first order Bessel function of the first kind, $k_0 = \omega/c$, $\rho = \sqrt{x^2 + y^2}$ is a radial distance, $\alpha_{1,2}$ are coefficients of the eigenmodes contributions. Next, using the approximation for the field profile inside the particle, we analyze the multipolar composition of the SH radiation generated by the nonlinear source following the procedure described in Ref. [25]. We deduce that the orbital numbers l of generated multipoles are even for electric and odd for magnetic multipoles, while the azimuthal number takes the values $m = \pm 2$ only. We find four dominant generated multipoles: $a_M^{(2\omega)}(2, \pm 2)$, $a_M^{(2\omega)}(4, \pm 2)$, $a_E^{(2\omega)}(3, \pm 2)$, $a_E^{(2\omega)}(5, \pm 2)$. Our analytical calculations show that at $k_0 r \sim 1$ electric multipolar coefficients $a_E^{(2\omega)}(l, \pm 2)$ rapidly decrease for $l \geq 7$, while magnetic amplitudes $a_M^{(2\omega)}(l, \pm 2)$ decay fast for $l \geq 6$. For example, in the vicinity of the BIC point we obtain the following relations in the case of AP beam excitation:

$$\left|\frac{a_E^{(2\omega)}(7, \pm 2)}{a_E^{(2\omega)}(5, \pm 2)}\right| \sim 0.02, \quad \left|\frac{a_M^{(2\omega)}(6, \pm 2)}{a_M^{(2\omega)}(4, \pm 2)}\right| \sim 0.08. \tag{11}$$

In the case when a nanoantenna supports both a quasi-BIC resonance near the pump frequency and an eigenmode near the SH frequency, we expect a resonant increase in the up-conversion. In addition to the eigenmodes at the fundamental frequency, Figure 4 features the dispersion of the high-quality mode at the second-harmonic frequency lying in the same range of parameters (SH mode). The *Q*-factor of this mode is large ($Q \approx 200 - 600$) (see Supplementary Material). Both Figures 2 and 4 show two interacting modes responsible for the quasi-BIC formation at the fundamental frequency and selected SH mode which falls in the same parameters' range and, by symmetry, can be excited by the BIC-driven nonlinear source. Certainly, there are several eigenmodes at the second-harmonic frequency in the considered range of parameters. However, here we specifically focus on the eigenmode that can be addressed by our nonlinear source $\mathbf{j}^{(2\omega)} = 2i\omega\mathbf{P}^{(2\omega)}$, namely, only the eigenmode with azimuthal indices $m = \pm 2$. This mode is composed of the multipoles that the induced nonlinear current at the quasi-BIC conditions generates. The multipolar decomposition of the SH mode is visualized by circles of different colors. The right inset additionally shows relative contributions of multipoles in the line plot. The SH mode has a more complex multipolar content than the FF modes, and a more sophisticated near-field distribution (top inset), which modifies slightly in the considered parameter range. The radiation pattern of the SH mode is generally multi-lobed and noticeably changes depending on the multipolar
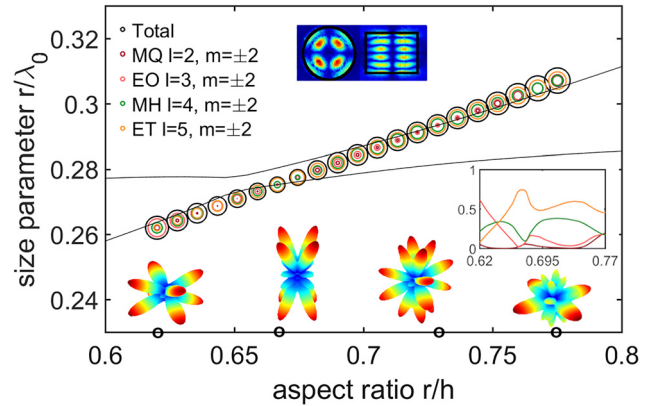

Figure 4: Colored circles trace dispersion of the eigenmode of the AlGaAs disk at the second-harmonic frequency (similar to Figure 2, its wavelength is doubled). Sizes of circles scale the total radiative decay (black) and partial multipolar contributions, also plotted as lines in the inset. Black solid lines are dispersion curves of the fundamental-frequency eigenmodes from Figure 2. Insets show the near-field distribution of the electric field magnitude at $r/h = 0.729$ (top and side views in the upper image) and far-field diagrams at $r/h = 0.62, 0.667, 0.729$ and 0.775 (the bottom row). E/M – electric/magnetic multipoles, Q – quadrupole, O – octupole, H – hexadecapole, T – triacontadipole.

composition. The most efficient SHG can be reached at the resonant conditions, close to the dispersion crossing of the quasi-BIC mode and the SH mode.

As a pump, we choose an AP beam in order to maximize the overlaps of the modes with the incident field. We numerically calculate dependencies of multipolar compositions of the linear scattering and SH radiation on the disk radius in the case of AP beam excitation (for comparison with the case of PW excitation see Supplementary Material). The multipolar contents of both FF and SH fields are found to be in excellent agreement with the results of our theory that justifies its validity. Figure 5 shows two-dimensional maps of linear scattering of the AP beam and the SH power. We recover maps of linear scattering, MD and MO contributions in linear scattering on the nanodisk radius by calculating slices at fixed pump wavelengths. We observe strong excitation of a magnetic octupole (MO) in the proximity of the BIC point so that the high-*Q* mode branch can be clearly traced in the map of linear scattering. Next, we model SHG and obtain a sharp enhancement peak in the SH intensity. The resonant area in the parameter space is visualized with high contrast in Figure 5D. These our results fully explain the recent experimental observations reported in Refs. [39, 40].

Figure 6 shows two slices of 2D color maps in Figure 5 for two close wavelengths: the slice at $\lambda_0 = 1580$ nm contains the BIC point and the slice at $\lambda_0 = 1600$ nm contains
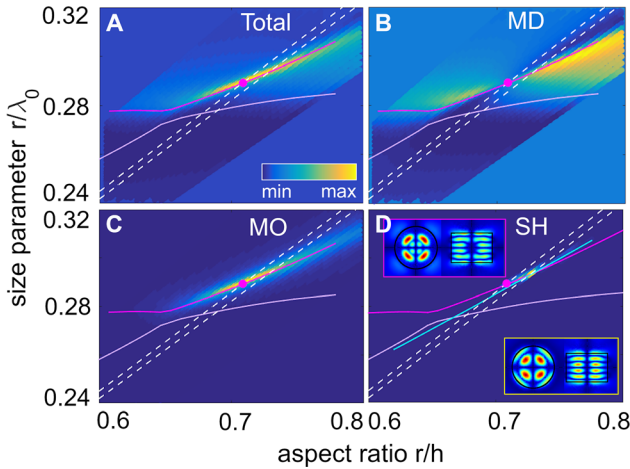
the intersection of the SH and FF dispersion curves. If we consider the fixed pump wavelength $\lambda_0 = 1580$ nm, we see that MO dominates in the linear scattering and the maxima of the scattering cross-section and the SH power for this slice correspond to the BIC point ($r = 457$ nm, $h = 645$ nm). We obtain that in this case magnetic quadrupole (MQ) $a_M^{(2\omega)}(2, \pm 2)$ dominates the emission, and the SH radiation pattern is mainly quadrupolar. For the wavelength $\lambda_0 = 1600$ nm corresponding to the intersection of the FF high-*Q* mode and SH mode dispersion branches, the SHG enhancement is even higher. In this case major multipoles are $a_M^{(2\omega)}(4, \pm 2)$, $a_E^{(2\omega)}(5, \pm 2)$, that matches the multipolar content of the SH mode.

Because the distribution of the AP beam intensity is inhomogeneous, here we define the scattering efficiency as the ratio of the scattering power at the fundamental frequency P_{FF} to the energy flux through the geometrical cross section of the particle in the waist plane P_{AP}:

$$\tilde{\sigma} = \frac{P_{FF}}{P_{AP}}, \tag{12}$$

$$P_{AP} = \int \overline{\mathbf{S}} \mathbf{n} dS = -\int \frac{E_\varphi H_\rho^* + E_\varphi^* H_\rho}{4} dS. \tag{13}$$

Here, $\overline{\mathbf{S}} = \frac{1}{2} Re(\mathbf{E} \times \mathbf{H}^*)$ is a time-averaged Poynting vector, $\mathbf{n} \parallel \hat{\mathbf{z}}$ is a normal vector. The scattering cross section $\sigma_{sca} = \tilde{\sigma} S$ is much larger than the geometric cross section S
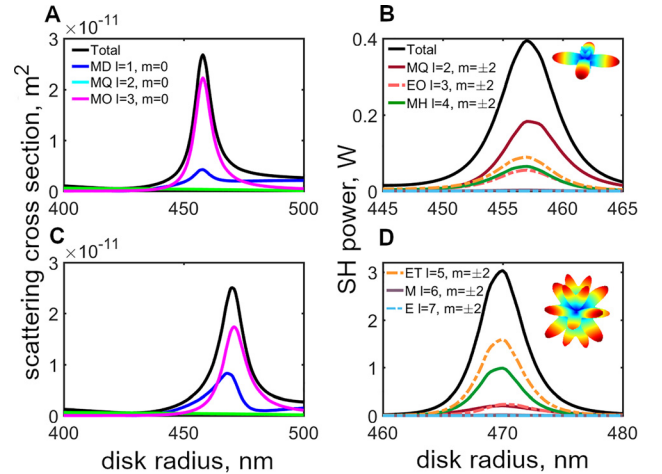

Figure 5: Maps of linear scattering of the AP beam by the AlGaAs nanodisk (A) and the SH generated power (D). Panels (B) and (C) correspond to magnetic dipole and octupole contributions to the linear scattering. Solid pink lines correspond to the dispersion curves of FF eigenmodes, solid blue line is the dispersion curve of SH mode. Pink dot marks a BIC state. Dashed lines are two slices of $\lambda_0 = 1580$ nm and $\lambda_0 = 1600$ nm. Insets in the panel (D) show electric field distribution at the BIC point (in the pink frame) and at point of intersections of dispersion curves (at maximum SH power) (in the yellow frame).

Figure 6: Multipolar decomposition of linear scattering (A,C) and second-harmonic generation (B,D) spectra for two slices in Figure 5. Top and bottom panels correspond to pump wavelengths $\lambda_0 = 1580$ and 1600 nm, respectively. Colored lines show different multipole contributions to the linear scattered and the second-harmonic fields. Insets show far-field diagrams of SH radiation at the BIC point ($\lambda_0 = 1580$ nm, $r = 457$ nm, $h = 645$ nm) and at the point of dispersion curves intersection ($\lambda_0 = 1600$ nm, $r = 470$ nm, $h = 645$ nm). E/M – electric/magnetic multipoles, D – dipole, Q – quadrupole, O – octupole, H – hexadecapole, T – triacontadipole.

($S = \pi r^2$ for AP and $S = 2rh$ for PW) of the disk near the BIC-point especially for the AP beam ($\sigma/\pi r^2 \approx 40$) because of the high-quality factor of the MO resonance. In this case, it would be incorrect to define the conversion efficiency as the ratio of the generated power P_{SH} and P_{AP} because these values become comparable near the BIC point. But the SH generated power is much smaller than the scattered power at the fundamental frequency because of the high-quality factor of the excited BIC mode. Thus, to take into account the strong interaction of the incident radiation with the resonant mode, we define the SH conversion efficiency as the ratio of the total SH radiated power P_{SH} to the radiated power at the fundamental frequency P_{FF}:

$$\rho = \frac{P_{SH}}{P_{FF}}. \tag{14}$$

We obtain that the absolute maximum of SHG corresponds to the intersection point and ideally, it may reach about 1% conversion. Also we calculate the conversion efficiency that doesn't depend on the incident power

$$\tilde{\rho} = \frac{P_{SH}}{P_{FF}^2}. \tag{15}$$

The coupled-mode considerations suggest scaling the SHG efficiency (15) depending on detunings from the resonances at the fundamental and SH frequencies:

$$\tilde{\rho} \sim Q_{FF}^2 Q_{SH} \left(\frac{\gamma_{FF}^2}{(\omega - \omega_{FF})^2 + \gamma_{FF}^2} \right)^2 \frac{\gamma_{SH}^2}{(2\omega - \omega_{SH})^2 + \gamma_{SH}^2}. \tag{16}$$

Here, Q_{FF} and Q_{SH} are quality factors of resonances, ω_{FF} and ω_{SH} are resonance frequencies, γ_{FF} and γ_{SH} are damping constants. The highest yield of SHG can be attained in the double-resonant case.
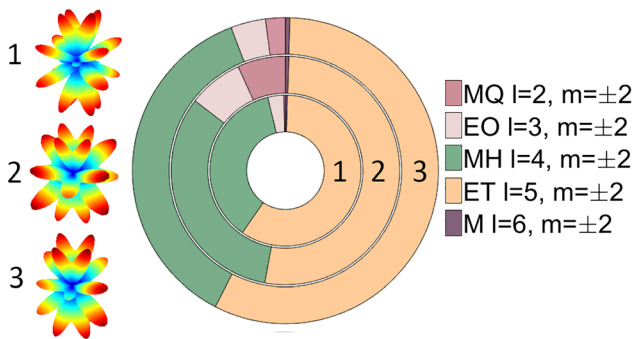

Figure 7: Comparison of the far-field diagrams and multipolar compositions of the SHG electromagnetic field and the disk's eigenmode at the SH frequency for parameters of the maximum SHG efficiency (λ_0=1600 nm, r=470 nm, h=645 nm): 1 - SH mode, 2 - AP beam excitation, 3 - PW excitation. E/M−electric/magnetic multipoles, Q−quadrupole, O−octupole, H−hexadecapole, T−triacontadipole

We compare near-field profiles, far-field diagrams and multipolar compositions of the SH mode and the SH radiation near the peak SHG for two types of incident radiation. We obtain that at the parameters of the maximum SHG, the multipolar composition of the SH generated field, the SH electric field distribution and the SH radiation pattern are almost the same as those of the SH eigenmode, see Figures 4, 5 and 7. This explicitly shows that even though the generated SH radiation is composed of several different multipoles, the only one SH mode characterized by $m = \pm 2$ is predominantly generated.

2.3 Coupled model of SHG with pump depletion

In our numerical modeling, we take into account the nonlinear effects of back-action of the second-harmonic radiation on the fundamental frequency radiation. In the case of highly efficient double-resonant excitation, the electric field amplitudes inside the particle at the fundamental and second-harmonic frequencies may become comparable, and the nonlinear correction of the polarization $\mathbf{P}_{nl}^{(\omega)}$ at the fundamental frequency can no longer be neglected. Thus, to simulate the back-action nonlinear effect, we numerically solve the Helmholtz equation for the electric field with nonlinear sources at the fundamental and SH frequencies simultaneously:

$$-\Delta \mathbf{E} + \mu_0 \frac{\partial^2 \mathbf{D}}{\partial t^2} = -\mu_0 \frac{\partial^2}{\partial t^2} \left(\mathbf{P}_{nl}^{(\omega)} + \mathbf{P}_{nl}^{(2\omega)} \right). \tag{17}$$

The expression for the nonlinear polarization at the fundamental frequency $\mathbf{P}_{nl}^{(\omega)}$ in the principle crystalline axis system has the following form:

$$\begin{pmatrix} P_{nlx}^{(\omega)} \\ P_{nly}^{(\omega)} \\ P_{nlz}^{(\omega)} \end{pmatrix} = 2\varepsilon_0 \chi^{(2)} \begin{pmatrix} E_y^{(2\omega)} E_z^{(\omega)*} + E_z^{(2\omega)} E_y^{(\omega)*} \\ E_x^{(2\omega)} E_z^{(\omega)*} + E_z^{(2\omega)} E_x^{(\omega)*} \\ E_x^{(2\omega)} E_y^{(\omega)*} + E_y^{(2\omega)} E_x^{(\omega)*} \end{pmatrix}. \tag{18}$$

The nonlinear source at the second-harmonic frequency is given by Eq. (8).

In the conditions of the resonant excitation of the magnetic-octupole quasi-BIC mode and the high-quality mode at the second-harmonic frequency, the electric field can be represented as a superposition

$$\mathbf{E} = \epsilon_1(t)\boldsymbol{\epsilon}_1(\mathbf{r})e^{i\omega_1 t} + \epsilon_2(t)\boldsymbol{\epsilon}_2(\mathbf{r})e^{i\omega_2 t} + c.c., \tag{19}$$

where $\epsilon_{1,2}(t)$ are the time-dependent amplitudes, $|\epsilon_{1,2}|^2$ are the energies of the modes at the frequencies $\omega_{1,2}$,

$\Delta\omega = \omega_2 - 2\omega_1$, $|\Delta\omega| \ll \omega_{1,2}$ is a detuning from the synchronism. Assuming the amplitudes slowly varying in time, with the characteristic time scale $\tau = \left|\frac{1}{\epsilon_{1,2}}\frac{d\epsilon_{1,2}}{dt}\right|^{-1} \gg \frac{2\pi}{\omega_{1,2}}$, one can write truncated equations

$$\frac{\partial\epsilon_1}{\partial t} + \overline{\gamma}_1\epsilon_1 = -i\overline{\chi}\epsilon_2\epsilon_1^* e^{i\Delta\omega t} + \sqrt{\overline{\gamma}_1}S_0 e^{i\Omega t},$$
$$\frac{\partial\epsilon_2}{\partial t} + \overline{\gamma}_2\epsilon_2 = -i\overline{\chi}^*\epsilon_1^2 e^{-i\Delta\omega t},$$
(20)

where the coefficient

$$\overline{\chi} \sim 2\omega\chi^{(2)} \int \left(\epsilon_{1y}\epsilon_{1z}\epsilon_{2x}^* + \epsilon_{1x}\epsilon_{1z}\epsilon_{2y}^* + \epsilon_{1x}\epsilon_{1y}\epsilon_{2z}^*\right)d^3\mathbf{r} \quad (21)$$

is proportional to the overlap integral, $\overline{\gamma}_{1,2}$ are decay rates of the quasi-BIC and SH modes.

We calculate the scattering and SHG conversion efficiencies taking into account coupling of the excited SH and FF modes and compare them with the numbers obtained in the undepleted pump approximation. The results for two types of incident radiation for parameters corresponding to the maximum SHG efficiency ($\lambda_0 = 1600$ nm, $r = 470$ nm, $h = 645$ nm) are summarized in Table 1.

Values of the pump intensity and the energy flux through the geometric cross section of the disk used in our calculations are given in Table 2. S denotes the geometrical cross section of the particle. In the case of AP beam excitation, I_{min} and I_{max} are the minimum and the maximum values of the total field intensity of the AP beam in the focal plane, P is the energy flux through the geometrical cross section of the particle in the focal plane. The characteristics of AP beam are illustrated in Fig. S3 of Supplementary Material. The plane-wave intensity $I_{min} = I_{max}$ is spatially constant. Taking into account a finite pulse duration, we have refined the value of the total conversion efficiency $\tilde{\rho}$ for AP beam and compared it with data from experimental works [39, 40] (see Supplementary Material). The calculated total second-harmonic efficiency 9.5×10^{-5} W^{-1} for 2 ps lasers pulses is approximately twice higher than the estimate in Ref. [40] based on the experimental data.

We obtain that in the case of AP excitation, nonlinear effects of back-action become noticeable due to efficient excitation of the high-quality modes. Thus, coupling of electromagnetic fields at the fundamental and second-

harmonic frequencies should be taken into consideration when the conversion efficiency reaches 1%. In the case of PW excitation, the maximum SHG is also reached for the parameters corresponding to the intersection of the eigenmodes dispersion curves, however, the total generated power turns to be lower than in the case of the AP beam pump. As noted above, it can be explained using multipolar analysis of the incident radiation. The multipolar composition of the incident plane wave is more complicated than multipolar composition of the AP beam, the spectrum of linear scattering contains several multipoles with different values of the azimuthal index m. As a result, the electric field distribution at the BIC point is distorted and appears dependent on the azimuthal angle φ. We still observe a resonance at the BIC point in the linear scattering spectrum but the corresponding scattering efficiency is an order of magnitude lower than in the case of AP excitation. Since the magnetic octupolar relative contribution with $m = 0$ is smaller in the plane wave, the excitation of the quasi-BIC state is less efficient.

In the next section, we consider the BIC-inspired nanoantenna design where the second-harmonic radiation significantly influences the linear scattering. Such nanoresonators can be particularly promising for realization of the efficient frequency downconversion at the nanoscale.

2.4 BIC-inspired nonlinear enhancement in a hybrid metal-dielectric nanoantenna

One type of BICs which has been widely studied is the symmetry-protected BIC occurring at Γ point of the bandstructure of a periodic leaky lattice. In periodic systems, when coupling of a certain resonance to the radiation modes is forbidden by a symmetry mismatch, a symmetry-protected BIC is formed [32, 41]. Such symmetry-protected BICs cannot be excited directly under normal plane wave incidence, while they can be excited externally by breaking the in-plane C_2 symmetry of the system, for example, by introducing a defect in the nanodisks to open a radiation channel and transform the ideal BIC to the quasi-BIC with a finite Q-factor [42]. In particular, by properly designing a nanodisk metasurface, it can support the longitudinal

Table 1: Scattering and second-harmonic conversion efficiencies.

	$\tilde{\sigma}$	ρ	$\tilde{\rho}$, W^{-1}
AP undepleted pump	34.14	0.02	1.33·10^{-4}
AP back-action	32.93	0.0182	1.25·10^{-4}
PW undepleted pump	3.97	0.0031	5.49·10^{-5}
PW back-action	3.95	0.0031	5.44·10^{-5}

Table 2: Pump characteristics.

	$I_{min}, \frac{GW}{cm^2}$	$I_{max}, \frac{GW}{cm^2}$	$S \cdot 10^{13}$, m^2	P, W
AP	0.89	2.16	6.94	4.404
PW	2.37	2.37	6.06	14.36

magnetic dipole resonance at Γ point at the frequency below the diffraction cut-off. Such MD mode does not couple to the free-space radiation forming a BIC. For isolated nano-resonators and nanoparticle oligomers, the out-of-plane Mie-type magnetic modes can be excited efficiently via an azimuthally polarized beam [43, 44, 45]. For periodic systems, this way is not feasible because the incident radiation in each unit cell has to be a structured field. However, inspired by the symmetry-protected BIC mechanism, here we suggest a novel approach to design and access the high-quality modes in isolated Mie nanoresonators.

A schematic illustration of the proposed principle is shown in Figure 8A. As was described in Ref. [16], when an electric current is placed near a perfect-electric-conductor (PEC) surface, the excited free electron oscillations in the adjacent PEC affect the near-field and far-field properties of such composite system. The effect can be reproduced with an oppositely oriented image of the electric current by using the image dipole model. Using this analogy, a periodic system of MD resonators can be transformed to a single MD resonator surrounded by a PEC-like box. As an example, we employ a dielectric disk surrounded by gold (Au) nanobars, as shown in Figure 8B. Remarkably, by shrinking a periodic system into a single nanoresonator, the quasi-BIC modes can be directly and efficiently excited under structured beam illumination that facilitates nonlinear frequency conversion.

We then take the AlGaAs nanodisk supporting a magnetic dipole resonance near 1550 nm and study the nonlinear performance of our proposed design. The geometric parameters of our structure are determined to be the following: the radius and height of AlGaAs nanodisk are r_0 = 237.5 nm, h_0 =400 nm; the length, height, and thickness of the gold structure are L =575 nm, $h_2 = 2h_0$, and t =100 nm. We suppose that an azimuthally polarized beam, with the maximum intensity I_{max} = 2.16 GW/cm^2, focused by an objective with the numerical aperture NA= 0.9 is illuminating our sample. Our recent experimental study [16] ensures that the pump intensities ∼3 GW/cm^2 do not cause damage of gold in the near-infrared range at the 1–2 ps laser pulse duration. Figure 8B shows the numerically computed linear scattering featuring magnetic multipoles with m = 0. A narrow dip appears around 1550 nm corresponding to excitation of the high-*Q* mode. The quality factor of this cavity mode is estimated to be Q = 554 which is much larger than that of typical MD resonance supported by an individual nanoresonator with ($Q∼$ 9) [22]. Its longitudinal nature enables optimal overlapping with an AP pump.
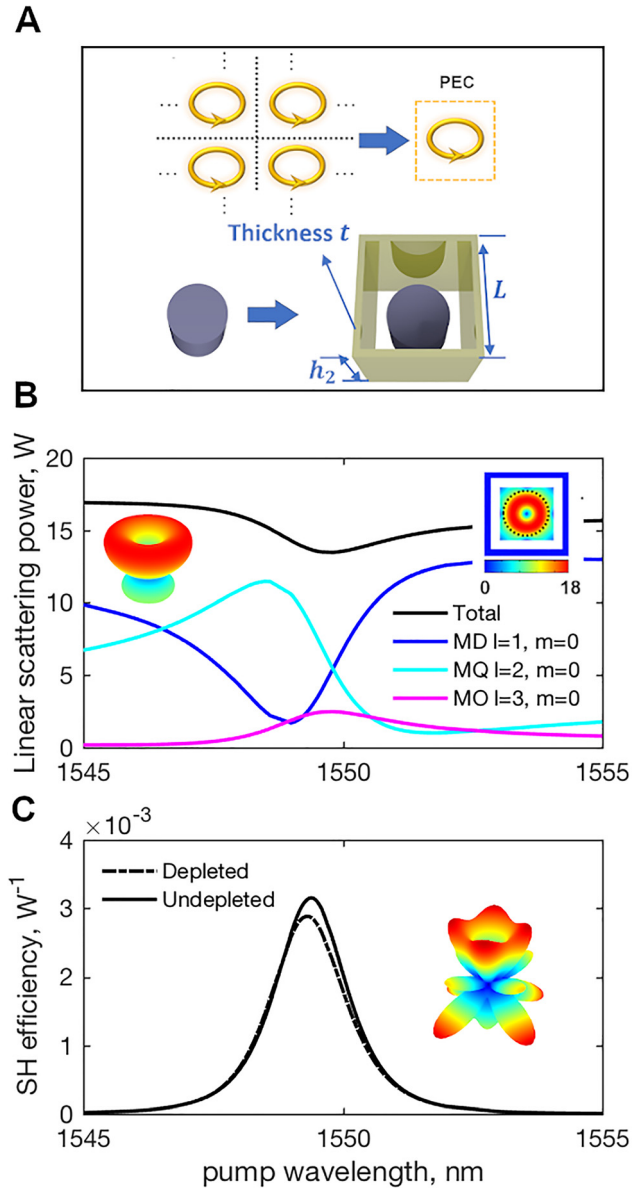

Figure 8: (A) Top: Schematic of the equivalent transformation between circular polarization currents excited in a periodic lattice of MD resonators and currents excited in a single MD resonator surrounded by PEC structures. Bottom: The transformation from a 2D periodic array of MD resonators to an isolated nanostructure composed of an MD resonator surrounded by gold nanobars. (B) Linear scattering and its multipolar decomposition for the hybrid AlGaAs-disk-with-Gold nanostructure under AP pump illumination. (C) SHG efficiency calculated using the undepleted pump model (solid line) and the coupled nonlinear model with back-action (dashed line). Inset shows the SH radiation pattern at the resonance.

We further examine the SHG process from the designed AlGaAs-Gold hybrid nanoresonator. In order to show the importance of our advanced simulation method introduced in Section 2.3, we compare the calculated results

based on the undepleted pump and the coupled back-action models in Figure 8C.

In the undepleted pump model, we follow two steps to simulate the nonlinear response. First, we calculate the linear response at the fundamental wavelength and obtain the nonlinear polarization induced inside the structure based on Eq. (8). We then employ the nonlinear polarization as a source to simulate the electromagnetic response at the harmonic wavelength. In this two-step procedure, we disregard the influence of the harmonic waves on the pump field. As seen in Figure 8C, the SHG emission is significantly enhanced when exciting the designed high-Q resonance at the pump frequency. Near the resonance, we observe a clear difference in the nonlinear emission power when using the coupled back-action model as compared to the undepleted pump model: at the pump wavelength of 1549 nm, the total SHG power is around 0.593 W and 0.546 W for these two cases, respectively. This indicates that neglecting coupling from SH field to the pump field in the undepleted pump model results in more than 8% error in the nonlinear simulation. Under AP pump illumination, the SHG signal can be boosted in our proposed configuration leading to nearly 2000-fold enhancement of the SHG emission power as compared to the case of SHG driven by the conventional MD resonance in a single free-standing nanodisk.

3 Conclusions

We have explicated the multipolar nature of quasi-BIC states in subwavelength dielectric resonators supporting high-quality supercavity modes called quasi-bound states in the continuum and discussed their applications for nonlinear nanophotonics. Using our multipolar model, we have analyzed optimal conditions for the efficient excitation of quasi-BIC states in high-index dielectric nanodisks under structured light illumination. In particular, we have explained the multifold increase of the second-harmonic conversion efficiency for the case of azimuthally polarized cylindrical vector beam illumination compared to the linearly polarized plane wave excitation. Implementing numerically the coupled nonlinear model, we have computationally refined values of SHG efficiencies and discussed pump depletion in high-quality nanoresonators.

References

[1] L. Novotny and N. van Hulst, "Antennas for light," *Nat. Photonics*, vol. 5, no. 2, pp. 83–90, 2011.

[2] L. Novotny and B. Hecht, Eds. *Principles of Nano-optics*. Cambridge University Press, 2012.

[3] V. M. Menon, L. I. Deych, and A. A. Lisyansky, "Nonlinear optics: towards polaritonic logic circuits," *Nat. Photonics*, vol. 4, no. 6, pp. 345–346, 2010.

[4] D. Smirnova and Y. S. Kivshar, "Multipolar nonlinear nanophotonics," *Optica*, vol. 3, no. 11, pp. 1241–1255, 2016.

[5] A. I. Kuznetsov, A. E. Miroshnichenko, M. L. Brongersma, Y. S. Kivshar and B. Lukyanchuk, "Optically resonant dielectric nanostructures," *Science*, vol. 354, p. 2472, 2016.

[6] M. R. Shcherbakov, P. P. Vabishchevich, A. S. Shorokhov, et al., "Ultrafast all-optical switching with magnetic resonances in nonlinear dielectric nanostructures," *Nano Lett.*, vo. 15, no. 10, pp. 6985–6990, 2015.

[7] M. R. Shcherbakov, S. Liu, V. V. Zubyuk, et al., "Ultrafast all-optical tuning of direct-gap semiconductor metasurfaces," *Nat. Commun.*, vol. 8, no. 1, p. 17, 2017.

[8] G. Li, S. Zhang and T. Zentgraf, "Nonlinear photonic metasurfaces," *Nat. Rev. Mater.*, vol. 2, p. 17010, 2017.

[9] S. Keren-Zur, L. Michaeli, H. Suchowski and T. Ellenbogen, "Shaping light with nonlinear metasurfaces," *Adv. Opt. Photonics*, vol. 10, no. 1, pp. 309–353, 2018.

[10] M. Rahmani, G. Leo, I. Brener, et al., "Nonlinear frequency conversion in optical nanoantennas and metasurfaces: materials evolution and fabrication," *Opto-Electron. Adv.*, vol. 1, p. 180021, 2018.

[11] B. Sain, C. Meier, T. Zentgraf, "Nonlinear optics in all-dielectric nanoantennas and metasurfaces: a review," *Adv. Photon*, vol. 1, p. 024002, 2019.

[12] M. R. Shcherbakov, D. N. Neshev, B. Hopkins, et al., "Enhanced third-harmonic generation in silicon nanoparticles driven by magnetic response," *Nano Lett.*, vol. 14, no. 11, pp. 6488–6492, 2014.

[13] L. Carletti, A. Locatelli, O. Stepanenko, G. Leo and C. De Angelis, "Enhanced second-harmonic generation from magnetic resonance in AlGaAs nanoantennas," *Opt. Express*, vol. 23, no. 20, p. 26544, 2015.

[14] L. Xu, M. Rahmani, D. Smirnova, et al., "Highly-efficient Longitudinal Second-harmonic Generation from Doubly-resonant AlGaAs Nanoantennas," in *Photonics*, Multidisciplinary Digital Publishing Institute, 2018, vol. 5, p. 29.

[15] A. E. Miroshnichenko, A. B. Evlyukhin, Y. F. Yu, et al., "Nonradiating anapole modes in dielectric nanoparticles," *Nat. Commun.*, vol. 6, p. 8069, 2015.

[16] L. Xu, M. Rahmani, K. Zangeneh Kamali, et al., "Boosting third-harmonic generation by a mirror-enhanced anapole resonator," *Light: Sci & Appl.*, vol. 7, p. 44, 2018.

[17] K. V. Baryshnikova, D. A. Smirnova, B. S. Luk'yanchuk and Y. S. Kivshar, "Optical anapoles: concepts and applications," *Adv. Opt. Mater.*, vol. 7, no. 14, p. 1801350, 2019.

[18] Y. Yang, W. Wang, A. Boulesbaa, et al., "Nonlinear fano-resonant dielectric metasurfaces," *Nano Lett.*, vol. 15, no. 11, pp. 7388–7393, 2015.

[19] A. S. Shorokhov, E. V. Melik-Gaykazyan, D. A. Smirnova, et al., "Multifold enhancement of third-harmonic generation in dielectric nanoparticles driven by magnetic fano resonances," *Nano Lett.*, vol. 16, no. 8, pp. 4857–4861, 2016.

[20] S. Kruk, A. Poddubny, D. Smirnova, et al., "Nonlinear light generation in topological nanostructures," *Nat. Nanotechnol.*, vol. 14, no. 2, p. 126, 2019.

[21] D. Smirnova, S. Kruk, D. Leykam, E. Melik-Gaykazyan, D. Y. Choi and Y. Kivshar, "Third-harmonic generation in photonic topological metasurfaces," *Phys. Rev. Lett.*, vol. 123, no. 10, p. 103901, 2019.

[22] G. Marino, A. S. Solntsev, L. Xu, et al., "Spontaneous photon-pair generation from a dielectric nanoantenna," *Optica*, vol. 6, no. 11, pp. 1416–1422, 2019.

[23] S. P. Rodrigues, S. Lan, L. Kang, Y. Cui, W. Cai, "Nonlinear imaging and spectroscopy of chiral metamaterials," *Adv. Mater.*, vol. 26, no. 35, pp. 6157–6162, 2014.

[24] D. A. Smirnova, A. B. Khanikaev, L. A. Smirnov and Y. S. Kivshar, "Multipolar third-harmonic generation driven by optically induced magnetic resonances," *ACS Photonics*, vol. 3, no. 8, pp. 1468–1476, 2016.

[25] D. Smirnova, A. I. Smirnov and Y. S. Kivshar, "Multipolar second-harmonic generation by Mie-resonant dielectric nanoparticles," *Phys. Rev.*, vol. 97, 2018. https://doi.org/10.1103/physreva.97.013807.

[26] K. Frizyuk, I. Volkovskaya, D. Smirnova, A. Poddubny and M. Petrov, "Second-harmonic generation in Mie-resonant dielectric nanoparticles made of noncentrosymmetric materials," *Phys. Rev.*, vol. 99, 2019. https://doi.org/10.1103/physrevb.99.075425.

[27] S. S. Kruk, R. Camacho-Morales, L. Xu, et al., "Nonlinear optical magnetism revealed by second-harmonic generation in nanoantennas," *Nano Lett.*, vol. 17, no. 6, pp. 3914–3918, 2017.

[28] R. Camacho-Morales, M. Rahmani, S. Kruk, et al., "Nonlinear generation of vector beams from AlGaAs nanoantennas," *Nano Lett.*, vol. 16, no. 11, pp. 7191–7197, 2016.

[29] M. K. Kroychuk, D. F. Yagudin, A. S. Shorokhov, et al., "Tailored nonlinear anisotropy in mie-resonant dielectric oligomers," *Adv. Opt. Mater.*, vol. 7, no. 20, p. 1900447, 2019.

[30] J. D. Sautter, L. Xu, A. E. Miroshnichenko, et al., "Tailoring second-harmonic emission from (111)-GaAs nanoantennas," *Nano Lett.*, vol. 19, no. 6, pp. 3905–3911, 2019.

[31] L. Xu, G. Saerens, M. Timofeeva, et al., "Forward and backward switching of nonlinear unidirectional emission from GaAs nanoantennas," *ACS Nano*, vol. 14, no. 2, pp. 1379–1389, 2020.

[32] C. W. Hsu, B. Zhen, A. D. Stone, J. D. Joannopoulos and M. Soljačić, "Bound states in the continuum," *Nat. Rev. Mater.*, vol. 1, p. 16048, 2016.

[33] M. V. Rybin, K. L. Koshelev, Z. F. Sadrieva, et al., "High-Q supercavity modes in subwavelength dielectric resonators," *Phys. Rev. Lett.*, vol. 119, no. 24, p. 243901, 2017.

[34] A. A. Bogdanov, K. L. Koshelev, P. V. Kapitanova, et al., "Bound states in the continuum and Fano resonances in the strong mode coupling regime," *Adv. Photonics*, vol. 1, no. 01, p. 1, 2019.

[35] W. Chen, Y. Chen and W. Liu, "Multipolar conversion induced subwavelength high-*Q* kerker supermodes with unidirectional radiations," *Laser Photonics Rev.*, vol. 13, no. 9, p. 1900067, 2019.

[36] L. Carletti, K. Koshelev, C. De Angelis and Y. Kivshar, "Giant nonlinear response at the nanoscale driven by bound states in the continuum," *Phys. Rev. Lett.*, vol. 121, no. 3, p. 033903, 2018.

[37] D. E. Aspnes, S. M. Kelso, R. A. Logan and R. Bhat, "Optical properties of AlxGa1-xAs," *J. Appl. Phys.*, vol. 60, no. 2, pp. 754–767, 1986.

[38] K. S. Youngworth and T. G. Brown, "Focusing of high numerical aperture cylindrical-vector beams," *Opt. Express*, vol. 7, no. 2, p. 77, 2000.

[39] K. Koshelev, S. Kruk, J. H. Choi, et al., "Observation of extraordinary SHG from all-dielectric nanoantennas governed by bound states in the continuum," *Conference on Lasers and Electro-Optics OSA2019*.

[40] K. Koshelev, S. Kruk, E. Melik-Gaykazyan, et al., "Subwavelength dielectric resonators for nonlinear nanophotonics," *Science*, vol. 367, no. 6475, pp. 288–292, 2020.

[41] Z. Sadrieva, K. Frizyuk, M. Petrov, Y. Kivshar and A. Bogdanov, "Multipolar origin of bound states in the continuum," *Phys. Rev. B.*, vol. 100, p. 115303, 2019.

[42] L. Xu, K. Z. Kamali, L. Huang, et al., "Dynamic nonlinear image tuning through magnetic dipole quasi-BIC ultrathin resonators," *Adv. Sci.*, vol. 6, no. 15, p. 1802119, 2019.

[43] T. Das, P. P. Iyer, R. A. DeCrescent and J. A. Schuller, "Beam engineering for selective and enhanced coupling to multipolar resonances," *Phys. Rev. B*, vol. 92, p. 241110, 2015.

[44] E. V. Melik-Gaykazyan, S. S. Kruk, R. Camacho-Morales, et al., "Selective third-harmonic generation by structured light in Mie-resonant nanoparticles," *ACS Photonics*, vol. 5, no. 3, pp. 728–733, 2017.

[45] M. K. Kroychuk, A. S. Shorokhov, D. F. Yagudin, et al., "Enhanced nonlinear light generation in oligomers of silicon nanoparticles under vector beam illumination," *Nano Lett.*, vol. 20, no. 5, pp. 3471–3477, 2020.